# Snaking without subcriticality: grain boundaries as non-topological defects

Priya Subramanian\*

Mathematical Institute, University of Oxford, Oxford OX2 6GG, UK

#### ANDREW J. ARCHER

Department of Mathematical Sciences and Interdisciplinary Centre for Mathematical Modelling, Loughborough University, Loughborough LE11 3TU, UK

#### EDGAR KNOBLOCH

Department of Physics, University of California at Berkeley, Berkeley, California 94720, USA

AND

#### Alastair M. Rucklidge

School of Mathematics, University of Leeds, Leeds LS2 9JT, UK \*Corresponding author: priya.subramanian@maths.ox.ac.uk

[Received on 2 November 2020; revised on 16 April 2021; accepted on 10 June 2021]

Non-topological defects in spatial patterns such as grain boundaries in crystalline materials arise from local variations of the pattern properties such as amplitude, wavelength and orientation. Such non-topological defects may be treated as spatially localized structures, i.e. as fronts connecting distinct periodic states. Using the two-dimensional quadratic-cubic Swift–Hohenberg equation, we obtain fully nonlinear equilibria containing grain boundaries that separate a patch of hexagons with one orientation (the grain) from an identical hexagonal state with a different orientation (the background). These grain boundaries take the form of closed curves with multiple penta-hepta defects that arise from local orientation mismatches between the two competing hexagonal structures. Multiple isolas occurring robustly over a wide range of parameters are obtained even in the absence of a unique Maxwell point, underlining the importance of retaining pinning when analysing patterns with defects, an effect omitted from the commonly used amplitude-phase description. Similar results are obtained for quasiperiodic structures in a two-scale phase-field model.

Keywords: non-topological defect; grain boundaries; penta-hepta defect; Swift-Hohenberg equation; spatial localization.

### 1. Introduction and motivation

Defects are of fundamental importance in the study of patterns as well as in materials science (Chaikin & Lubensky, 1995; Cross & Hohenberg, 1993; Mermin, 1979) and may take the form of domain walls, grain boundaries, dislocations and disclinations. These structures can be stationary or glide or climb or otherwise move through the pattern and are present in one, two and three dimensions. One traditional approach to the study of defects uses an amplitude-phase decomposition in which a periodic pattern is described by a homogeneous amplitude and defects are associated with zeros of the amplitude. Since the phase at these locations is undefined, these defects are known as topological defects and these have attracted the greatest attention (Mermin, 1979). Such defects are characterized by a non-zero topological charge, proportional to the integral of the phase around the defect. However, many defects are

non-topological in character but are nonetheless of fundamental significance (Chaikin & Lubensky, 1995). For these defects, the phase gradient is defined everywhere and the topological charge vanishes. Non-topological defects are frequently believed to be less important since isolated defects of this type may heal or otherwise disappear without interaction with another defect. However, this is not always the case, and if the defect has internal structure, it may persist as a result of frustration or locking to the background state.

In the present work, we adopt a different point of view and think of defects as spatially localized structures embedded in a background pattern. In general, defects represent a local disruption of the background state, and so can consist of holes where its amplitude is locally reduced, or local changes in the background wavenumber or its orientation. In most cases, the background state is a periodic or crystalline state, but defects in quasicrystals or even disordered media also arise (Korkidi *et al.*, 2013).

Spatial localization has been the subject of numerous recent studies (see Knobloch, 2015, for a review) leading to the following picture of such structures. Defects may be described as holes in a pattern and these bifurcate from a pattern branch near its folds and are initially unstable. Both of these facts are a consequence of the presence of a Floquet multiplier +1 at such folds. In variational systems, the resulting hole branch undergoes homoclinic snaking (Woods & Champneys, 1999) in the vicinity of a Maxwell point, the parameter value at which the free energy associated with the pattern is the same as that of a competing state. Homoclinic snaking is responsible for stabilizing some of the hole states and is a consequence of the locking of a front between the two competing states to the heterogeneity or spatial structure on one or both sides of the front. On the basis of this picture, we expect stable defect states to be present in regions of bistability, and associated with the presence of a Maxwell point, i.e. in the so-called snaking or pinning region. In particular, we expect holes to come in the form of infinite families of defect structures of specific symmetry and ever-increasing size, all of which coexist stably within the pinning region. In general, these structures either snake or lie on a stack of isolas (Beck et al., 2009). Much of the above picture has been developed on the basis of detailed studies of the bistable Swift-Hohenberg equation (Burke & Knobloch, 2006), a prototypical pattern-forming equation exhibiting bistability between a pattern state and a spatially homogeneous or flat state.

We point out that the traditional approach to analyse defects using an amplitude-phase decomposition ignores the possibility of pinning, thereby collapsing the family of defects to a stationary heteroclinic front at the Maxwell point. The present work shows that pinning must be retained in studies of defects and that its effects in general extend over a broad range of parameter values. To demonstrate the importance of pinning and the associated multiplicity of defect structures, we adopt the two-dimensional (2D) quadratic-cubic Swift–Hohenberg equation (SH23) and focus on one of the most important defect structures in 2D, the penta-hepta defect (PHD) in a hexagonal pattern. This classical structure consists of a bound state of a peak with five neighbours and a peak with seven neighbours, instead of the usual six neighbours in a defect-free hexagonal pattern. Figure 1 shows such a defect in a largely hexagonal arrangement of gannet nests at Muriwai beach in New Zealand.

In particular, we compute here three distinct defect structures and the associated isolas, thereby providing compelling evidence for the coexistence of multiple defect structures in 2D. Earlier work in 1D examined domain boundaries between two distinct spatially periodic states in SH357, the cubic-quintic-septic Swift–Hohenberg equation (Knobloch *et al.*, 2019), and confirmed the presence of defect snaking in one spatial dimension. Snaking of grain boundaries between stripe patterns with different orientations in 2D has been investigated in the Swift–Hohenberg equation with cubic nonlinearity (Lloyd & Scheel, 2017). In our work, we investigate the Swift–Hohenberg equation with quadratic and cubic nonlinearities in the supercritical regime where hexagonal patterns are stable. The PHDs we study are the result of a local change in the orientation of the hexagonal pattern. Thus, these defects are the





Fig. 1. When neighbours keep their distance: gannets nesting at Muriwai beach, New Zealand. The image on the left shows the overall hexagonal ordering of the birds while that on the right shows a PHD. The green (pink) markers identify gannets with five (seven) neighbours instead of the usual six. Photo credit: Barbora Knobloch.

result of bistability between a hexagonal pattern and a rotated version of the same pattern. We expect similar structures in mass-conserving systems described by the conserved Swift–Hohenberg equation, or equivalently the phase-field crystal (PFC) model, since stationary states of this model satisfy the same stationary equation as that studied below (Thiele *et al.*, 2013).

The bistable 2D SH23 equation describes competition between hexagonal patterns and a trivial, spatially homogeneous state. The equation is variational with a Maxwell point between the hexagonal state and the trivial state. For this reason, this equation admits both holes in a hexagonal pattern and hexagon patches embedded in the trivial background (Lloyd et al., 2008). Here we are interested in defects that are not associated with the trivial state and that are found in the supercritical regime. These defects are associated with grain boundaries between two hexagonal patterns, obtained by rotating the hexagonal pattern in part of the domain through 30 degrees relative to the rest. This procedure generates closed rings of PHDs. These are found to lie on distinct isolas despite the absence of a discrete Maxwell point between the two competing hexagonal states (both of which have the same free energy). We mention that an isolated PHD in a hexagonal pattern can be described using an amplitude-phase description (Tsimring, 1995). This description shows that such defects can be thought of as a bound state of two dislocations, of opposite signs, in two of the three Fourier modes involved in the basic hexagonal structure. Such defects can be stationary or can climb (Tsimring, 1995). However, the description of such motion is expected to be strongly influenced by the presence of pinning between the PHD and the surrounding hexagonal pattern. It is this effect that is responsible for the multiplicity of PHD structures in this system.

As already mentioned, equilibria of the Swift–Hohenberg equation are also equilibria of the PFC model, which is a simple theory for the crystallization of matter. In this context, the results presented below apply to defects observed at grain boundaries in polycrystalline materials. In particular, since we are considering a 2D system, our results apply to grain boundaries in 2D solids such as graphene (Hirvonen *et al.*, 2016, 2017), in which defects are of great importance close to melting (Zakharchenko *et al.*, 2011) and indeed affect the very nature of melting in 2D (Halperin & Nelson, 1978).

This paper is organized as follows. In the next section, we introduce the model equation we study and the demodulation technique we use to isolate the defect state. In Section 3, we describe our procedure for generating rings of PHDs. These structures are shown in Section 4 and found to lie on distinct isolas. The spatial extent of the influence of the resulting PHD structures on the background hexagonal pattern is quantified. The paper concludes with a brief summary and some questions concerning the implications of multiple equilibria with defects for both pattern formation and material science that will, we hope, inform future work.

### 2. Model and methodology

#### 2.1 The model

We consider the pattern-forming system SH23, a fourth-order partial differential equation for a scalar field  $u(\mathbf{x}, t)$ ,

$$\frac{\partial u}{\partial t} = \mu u - (1 + \nabla^2)^2 u + Q u^2 - u^3.$$
 (2.1)

For some background on this equation, see e.g. Burke & Knobloch (2006). The parameters in this model are the linear growth rate  $\mu$  and the strength Q>0 of the quadratic interactions. The domain chosen for all the calculations in this work, unless specified otherwise, is a periodic square with side length  $L_x=L_y=60\pi$  (30 wavelengths of the characteristic mode with wavenumber k=1), discretized with 256 grid points in each direction.

Equation (2.1) describes non-conserved gradient dynamics  $\partial u/\partial t = -\delta \mathcal{F}[u]/\delta u$ , with the free energy functional

$$\mathcal{F}[u] = \int \left[ -\frac{1}{2}\mu u^2 + \frac{1}{2}u(1+\nabla^2)^2 u - \frac{1}{3}Qu^3 + \frac{1}{4}u^4 \right] d\mathbf{x}.$$
 (2.2)

As a result, all initial conditions evolve towards steady states corresponding to (local) minima of  $\mathcal{F}[u]$ .

#### 2.2 Numerical details

Time stepping from a given initial condition is accomplished pseudospectrally using second-order exponential time differencing (ETD2) (Cox & Matthews, 2002). Numerical continuation is done using pseudo-arclength continuation similar to that employed in Subramanian *et al.* (2018). In particular, we use the Krylov space method of induced dimension reduction (Sonneveld & Gijzen, 2009) to compute the action of the 256<sup>2</sup> Jacobian matrix. For all computations in this paper, the dimension of the shadow space chosen is 8 and the required tolerance is set at  $tol_{idrs} = 3 \times 10^{-3}$ . The Newton iterations are considered to be converged if the current tolerance satisfies  $tol_{Newton} = (||correction||_2/||state||_2) < 10^{-10}$  and the convergence rate is quadratic in the last few Newton iterations.

In order to obtain such a quadratic convergence, we make use of a preconditioner to solve the linearized system. The preconditioner is based on  $\hat{\mathcal{L}}$  which is the Fourier transform of the linear operator

 $\mathcal{L}$  arising in (2.1), and defined by

$$\mathcal{M} = \begin{cases} 1, & \text{if } |\hat{\mathcal{L}}_{ij}| < tol_{\mathcal{M}}, \\ 1/\hat{\mathcal{L}}_{ij}, & \text{otherwise}. \end{cases}$$
 (2.3)

We have chosen the tolerance to be  $tol_{\mathcal{M}}=10^{-6}$  for all the computations. This allows us to approximate the perfect preconditioner of  $\mathcal{L}^{-1}$  for all parts that are not singular (Tuckerman & Barkley, 2000).

## 2.3 Spectral filtering

Figure 2(a) shows the bifurcation diagram of extended hexagonal states  $H^{\pm}$  (so-called up-hexagons and down-hexagons, respectively) as a function of the chosen bifurcation parameter  $\mu$  when Q=0.75. A transcritical bifurcation occurs at  $\mu=0$ , generating  $H^+$  for  $\mu<0$  and  $H^-$  for  $\mu>0$ . The  $H^+$  states undergo a saddle-node bifurcation at  $\mu=-0.05$ . Shown are two superposed branches differing in the orientation of their wavevectors in their Fourier spectrum. The blue line has solutions that include the wavevector (0,1), whose real space pattern is shown in panel (c) with a blue border and labelled  $u_{01}$ . Solutions along the dashed red line have wavevectors including (1,0) whose real space pattern is shown in panel (d) with a red border and labelled  $u_{10}$ . We observe that the root mean square norms of both these extended states are equal, as expected, since the patterns are just rotations of each other.

We can differentiate between the two extended hexagonal patterns if we consider one of them to be the reference state, say  $u_{01}$ , and measure the norm of the difference between a given state and  $u_{01}$ . In order to identify the parts of a given field u that differ from the chosen reference state, we create a filter matrix  $\mathcal{P}$  in spectral space from the reference state  $u_{01}$  in the following way.

First, we identify all the Fourier components that contribute non-trivially to the spectrum of the reference state by identifying the reciprocal lattice vectors (RLVs) of the reference state  $\hat{u}_{01}$ , including wavevectors that are obtained via higher-order interactions (see e.g. the discussion in Chaikin & Lubensky, 1995, Chapter 4). Figure 2(e) shows the locations of these wavevectors in the 2D domain as blue circles. The dashed-dotted circle has been added to help identify the order 1 RLVs of magnitude  $|\mathbf{k}|=1$ , the radius of the circle. In order to calculate the distance of a given state from this hexagonal pattern, we seek to set all contributions from the above Fourier components to zero in the pattern of interest. In this way, we define the projection  $\mathcal P$  whose application to the Fourier transform of a given field  $u(\mathbf{x})$  sets all the Fourier components identified in Fig. 2(b) to zero. The resulting field IFFT( $\mathcal P\hat u$ ), where IFFT denotes the inverse fast Fourier transform, is now spectrally filtered and has no components along the Fourier components of the reference field, in this case  $u_{01}$ .

If we consider the same extended hexagonal patterns as in Fig. 2(a) and replot them using the root mean square of the spectrally filtered state  $u_{fil}$ , calculated as

$$rms(u_{fil}) = \sqrt{\frac{1}{A} \int \left[ IFFT(\hat{\mathcal{P}u}) \right]^2 dA}, \qquad (2.4)$$

we obtain Fig. 2(b). Since the new measure  $rms(u_{fil})$  represents the departure of a pattern u from the chosen reference pattern, in this case  $u_{01}$ , the state  $u_{01}$  corresponds to the blue horizontal line with zero amplitude, while the state  $u_{10}$ , shown in red, remains unmodified at the scale of the figure (compare the red dashed lines in Fig. 2(a and b)). This is because in the case of extended periodic patterns, the higher-order contributions to the Fourier spectrum of the pattern  $u_{10}$  at wavevectors that are part of the

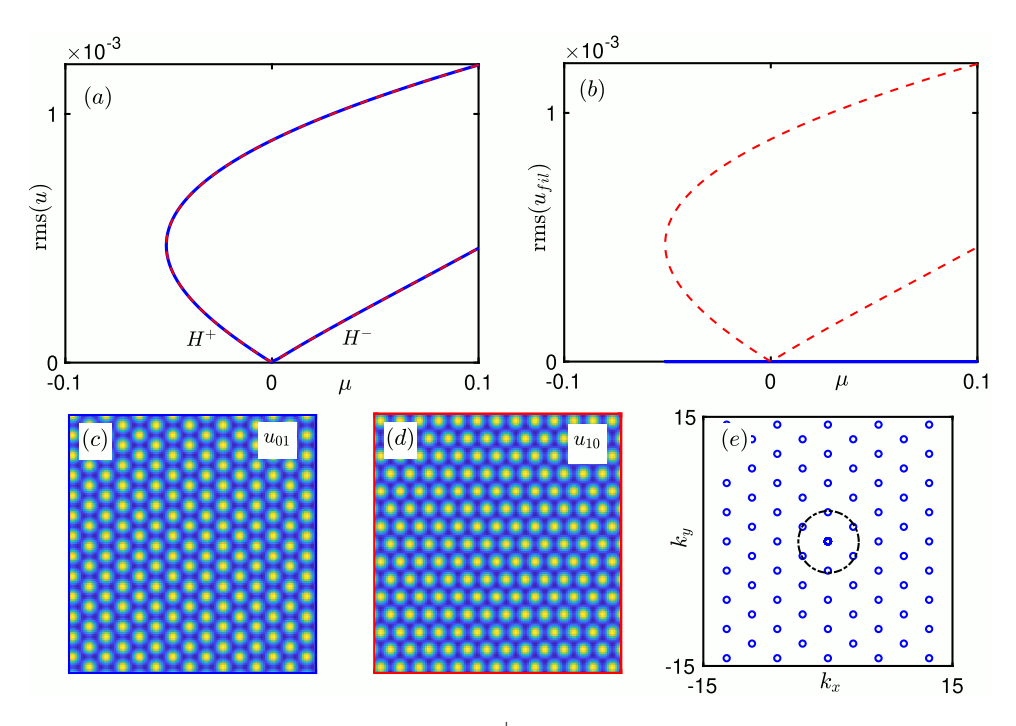


Fig. 2. (a) Bifurcation diagram of extended hexagonal states  $H^{\pm}$  showing the root mean square norm rms(u) as a function of the bifurcation parameter  $\mu$  computed for SH23 with Q=0.75. (b) The corresponding bifurcation diagram using the filtered norm rms( $u_{fil}$ ) for  $u_{10}$  (red) and  $u_{01}$  (blue). Panels (c) and (d) show the two different orientations of the extended hexagonal states of interest, the state  $u_{01}$  with blue border and the state  $u_{10}$  with red border; both have the same norm and correspond to solutions from the  $H^+$  branch at  $\mu=0.25$ . (e) Components of the RLVs of the state  $u_{01}$  which are set to zero in the filter  $\mathcal{P}$ , shown in a periodic domain of size 30 wavelengths (256 grid points) in each direction. The dashed-dotted black circle passes through the first order RLVs.

higher-order spectrum of the pattern  $u_{01}$  are very small. The largest change arises from the removal of the bulk mode at  $|\mathbf{k}| = 0$ . We mention that if the reference state is chosen to be the flat state, the measure (2.4) reduces to the usual rms(u).

In this section, we have introduced the idea of spectral filtering to help visualize states with defects. In the rest of this work, we focus on the formation of spatially localized patterns that involve PHDs separating the two hexagonal states  $u_{01}$  and  $u_{10}$ . However, the idea of spectral filtering to visualize defects is more general and can be used to describe more complex grain boundaries.

## 3. PHDs and grain boundaries

In the SH23 equation introduced in the previous section, we look for equilibria that involve PHDs. In order to promote the formation of hexagonal patterns, we set Q=0.75 and choose a positive value of the growth rate,  $\mu=0.25$ . To construct suitable initial conditions, we first compute the extended hexagonal states  $u_{01}$  and  $u_{10}$  and extract their amplitudes via a Fourier transform. The desired initial conditions consist of a patch of the converged state  $u_{10}$  in the background of the converged state  $u_{01}$  and we vary both the patch shape and its size. In order to have clean fronts between the patch and the background, the patch shapes consist of edges that are aligned with the 01 direction in Fourier space. In

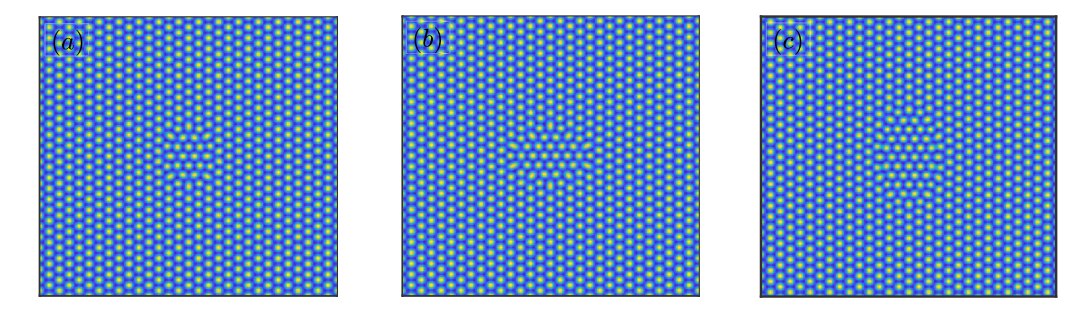


Fig. 3. Coexisting equilibria with PHDs separating regions of hexagons with different orientations in the SH23 system with parameters  $\mu = 0.25$  and Q = 0.75. All are dynamically stable states.

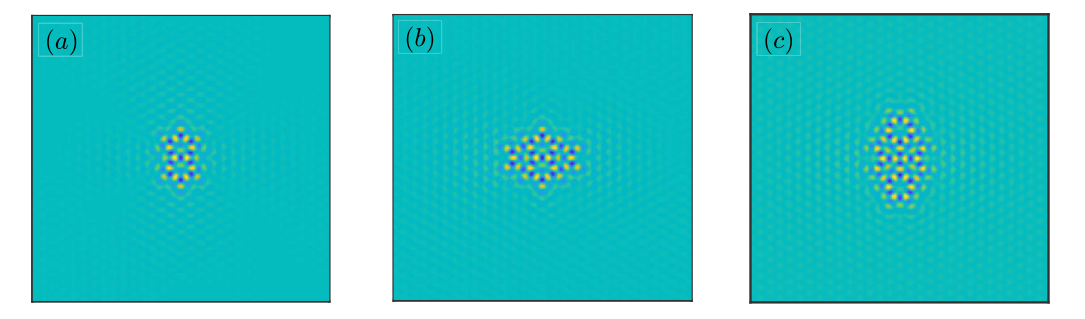
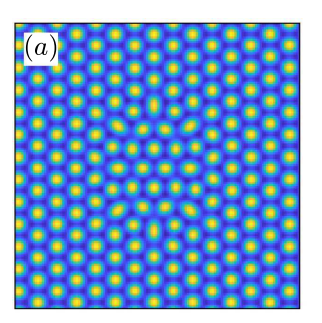


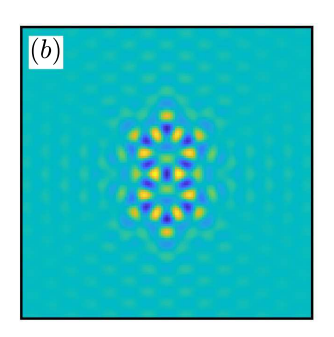
Fig. 4. Corresponding spectrally filtered fields of the patterns in Fig. 3 showing locations in the (x, y) plane with deviation from the background state  $u_{01}$ .

the simplest case, the patch shape that we consider is a hexagon of a given edge length oriented such that two opposing edges align with the 01 direction. Interpolation between the patch and background might help to create a smoother initial condition, but here we do not do this but instead use time stepping to examine if the initial condition is close to a stable equilibrium of the system by tracking its evolution. In most trials, our initial guess is not close to a stable equilibrium and the evolution approaches the fully extended hexagon state. However, identifying initial conditions that display slow changes in the norm of the field, i.e.  $(||u(t) - u(t - \Delta t)||_2)$ , helps us identify likely candidates for use in a Newton solver, regardless of stability. This combination of time stepping and numerical continuation has proved effective for computing multiple coexisting states that involve spatial localization of a patch of  $u_{10}$  within a  $u_{01}$  background. Figure 3 shows several such examples that are dynamically stable as confirmed by time-evolving small perturbations using (2.1).

Since it is difficult to identify visually the location of the defects in this state, we also look at the corresponding spectrally filtered fields  $u_{fil}$  in Fig. 4. Here we see that the regions in Fig. 3 that are purely hexagonal with orientation  $u_{01}$  are transformed into flat (green) regions in the spectrally filtered plot. Additionally, peaks in the  $u_{10}$  patch coinciding with those of  $u_{01}$  are also removed, see e.g. the flat/green regions in the middle of the hexagonal ring of peaks in Fig. 4(a). Note also that as we move across the three panels, the size of the  $u_{10}$  patch in the middle occupies a larger part of the domain. However, all of the cases shown here possess symmetry with respect to reflections in the x- and y-axes.

In order to correlate the location of the grain boundaries and associated PHDs in the *u* fields shown in Fig. 3 with the corresponding peaks in Fig. 4, we compare the two fields in panels (a): we zoom in to the





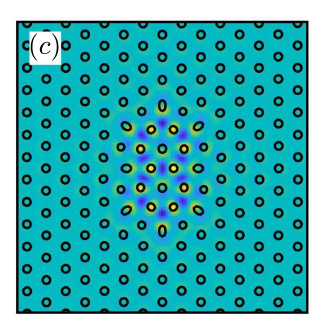


Fig. 5. (a) Zoomed-in view of the centre of the domain from Fig. 3(a) showing u(x, y). (b) Corresponding zoomed-in area from Fig. 3(a) showing  $u_{fil}$ . (c) Contours determined at 65% of max(u) from panel (a) shown in black, superposed on  $u_{fil}$  from panel (b).

centre of the domain in Fig. 3(a) and show the results in Fig. 5(a). Figure 5(b) shows the corresponding zoomed-in view of Fig. 4(a). In order to combine the information in both these figures, we estimate contours from panel (a) where the value of u is 65% of the maximum value over the domain. Then we superpose these contours (as black solid lines) over the  $u_{fil}$  field as shown in Fig. 5(c). We see that the black contours line up with the peaks in the patch of  $u_{10}$  while valleys between them, indicated in blue, indicate the locations of missing  $u_{01}$  peaks. It is also possible to discern distortions in the background  $u_{01}$  state in the vicinity of the grain boundary.

We seek to identify peaks that have five (seven) neighbours in order to locate PHDs automatically. In order to do this, we start with the data from the contours determined at 65% of  $\max(u)$  as seen in Fig. 5(c). We determine the grid  $\mathcal{G}$  comprised of the centres of each closed black circle (representing a single peak) in the contour. For points in the grid  $\mathcal{G}$ , we create a 2D Delaunay triangulation and use it to determine the number of neighbours which surround each point in  $\mathcal{G}$ . From this, we can immediately identify the locations of peaks that have five (seven) neighbours. Figure 6 reproduces Fig. 5(c) with additional green star markers indicating peaks with five neighbours and pink star markers indicating peaks with seven neighbours. This same procedure is adopted to create figures comprising the contours of the field u superposed on the image of  $u_{fil}$  and overlaid with the locations of the PHDs in the movies associated with this paper.

# 4. To snake or not to snake

Having obtained multiple states with PHDs as equilibria of the SH23 equation at a given parameter value (as shown in Fig. 3), we seek to understand if these states are connected via homoclinic snaking, i.e. if they lie on the same solution branch. In order to determine this, we perform numerical continuation (Doedel *et al.*, 1991) of the solutions of the equation

$$\mu u - (1 + \nabla^2)^2 u + Q u^2 - u^3 = 0, \qquad (4.1)$$

Here, as with time stepping, the field u is discretized in space and nonlinear terms are calculated pseudo-spectrally. Pseudo-arclength continuation is performed with variable stepsize along the solution branch using a biconjugate gradient-stabilized method (Vorst, 1992) to approximate the action of the Jacobian matrix of the system.

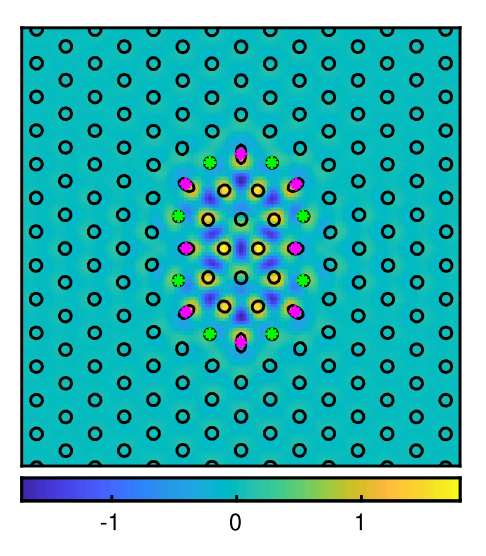


Fig. 6. Contours of u determined at 65% of  $\max(u)$  superposed on  $u_{fil}$ , reproduced from Fig. 5(c). The locations of PHDs are indicated using green star markers for peaks with five neighbours and pink star markers for peaks with seven neighbours.

We start with the state in Fig. 3(a) and vary the bifurcation parameter  $\mu$ . Figure 7(a) shows the complete isola in terms of rms( $u_{fil}$ ) plotted as a function of the bifurcation parameter  $\mu$  over the range  $0.032 < \mu < 0.41$ . Starting at  $\mu = 0.25$  and decreasing  $\mu$ , the measure rms( $u_{fil}$ ) decreases along the solution branch and the branch turns around at a saddle-node bifurcation at  $\mu \approx 0.032$ , followed by two further turning points at  $\mu \approx 0.189$  and  $\mu \approx 0.173$  before returning to the starting value of  $\mu = 0.25$ . In order to compare the states on the solution branch before and after the first saddle-node bifurcation, we pick two nearby values  $\mu = 0.1534$  and  $\mu = 0.1539$ , labelled (c) and (d) in Fig. 7(a), and display the corresponding fields  $u_{fil}$  in Fig. 7(c) and (d), respectively. Between these two solutions, the localized patch of PHDs has lost four peaks and has become slightly smaller. Such a change, involving addition/removal of part of the pattern across a saddle-node bifurcation, is similar to changes observed during homoclinic snaking of localized hexagon states in a u = 0 background in the subcritical regime  $\mu < 0$  (Lloyd *et al.*, 2008). In addition, the larger amplitude state (b) distorts the background state over a larger distance.

Supplementary material Movie 1 shows how  $rms(u_{fil})$  changes as we move over this isola. Note that the identification of peaks with five or seven neighbours is based on the 2D Delaunay triangulation, which is in turn based on the contours of the field u. This means that any asymmetry in the location of the associated PHDs we observe at multiple locations along the isola could be a consequence of two levels of discretization: one at the level of determining the centre of a contour peak and the second at the level of the automated determination of the number of nearest neighbours from the resulting 2D Delaunay triangulation.

In the next panel, Fig. 7(b), we see another version of the same bifurcation diagram with a different norm on the y-axis. In order to understand the relative cost in terms of free energy that is needed to create the observed ring of PHDs, i.e. to calculate the grain boundary free energy (Hirvonen *et al.*, 2016, 2017), we first determine the free energy,  $\mathcal{F}[u_{01}]$ , of the reference state  $u_{01}$  from (2.2). We subtract this free energy from the free energy,  $\mathcal{F}[u]$ , corresponding to the field in Fig. 3(a). With this difference in

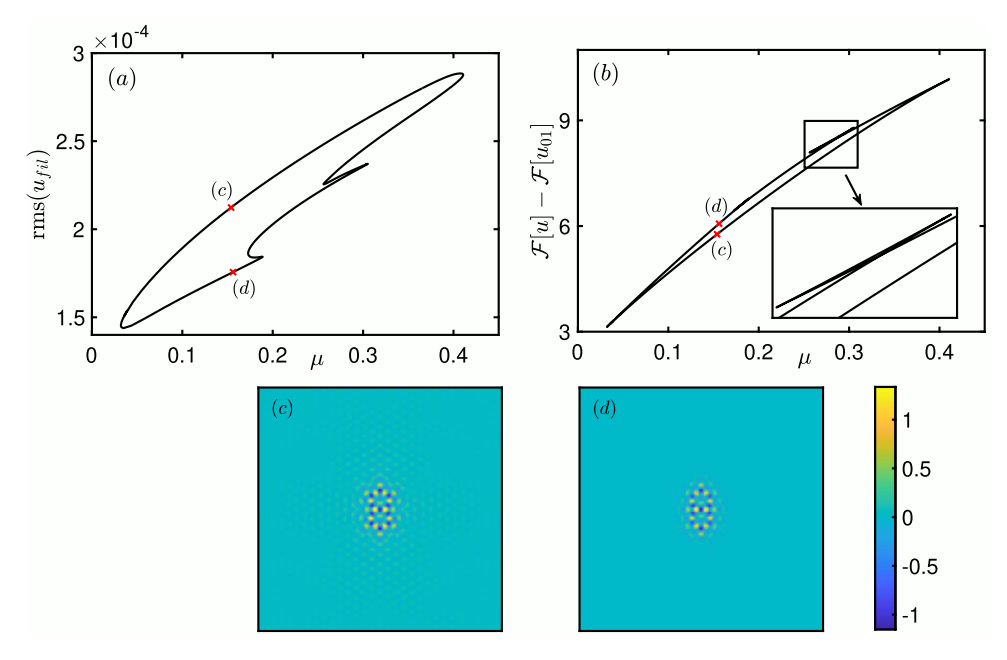


Fig. 7. Complete isola of the solution branch related to the field in Fig. 5(a) shown in terms of (a)  $rms(u_{fil})$  and (b) the free energy difference,  $\mathcal{F}[u] - \mathcal{F}[u_{01}]$ , both as functions of the bifurcation parameter  $\mu$ . The inset in (b) shows an enlargement of the region within the rectangle displaying swallow-tail behaviour in the solution branch.

free energy costs as our norm, the resulting isola is as shown in Fig. 7(b). As shown enlarged in the inset, this curve displays swallow-tail behaviour at locations where we observe two consecutive saddle-node bifurcations in Fig. 7(a). This result is similar to the occurrence of swallow-tail structures in the snaking of 2D quasicrystals in Subramanian *et al.* (2018). The difference in free energy, i.e.  $\mathcal{F}[u] - \mathcal{F}[u_{01}]$ , gives the free energy of the interface and shows that this increases with  $\mu$ , since the perimeter of the grain hardly changes as we go around the isola. Of course, the grain boundary free energy depends on the relative orientation (Hirvonen *et al.*, 2016) of the neighbouring grains, but this also does not change around the isola.

Figure 8 shows the consolidated version of the previous figure with the solution branches associated with all the three states shown in Fig. 4 for  $\mu=0.25$ . Panel 8(a) shows the variation of  $\mathrm{rms}(u_{fil})$  for the three isolas that result, all of which exist over a large range of the bifurcation parameter  $\mu$ . From this panel, we deduce a direct correlation between increased  $\mathrm{rms}(u_{fil})$  values and the size of the central patch. Figure 8(b) shows the variation of the free energy difference between a state with a closed ring of PHDs and the extended hexagonal pattern, for the three different isolas. All of these free energy differences are positive and increase with the perimeter of the central patch. We observe the presence of multiple swallow-tail like structures along the isolas and include an enlargement of one such swallow-tail from the isola connected to the solution in Fig. 3(b). In this figure, we also show additional solutions from each isola focusing on solutions at smaller values of  $\mu$ . The location of each solution is marked with a red circle in Fig. 8(a) and (b) and identified with the letters A–D. Compared to Fig. 6, we see that the variation of  $u_{fil}$  in these panels is reduced, as reflected in the smaller difference between the maximum and minimum value of  $u_{fil}$  in the associated colour bars. For a comprehensive look at how these solutions vary along different isolas, see the supplemental movie files.

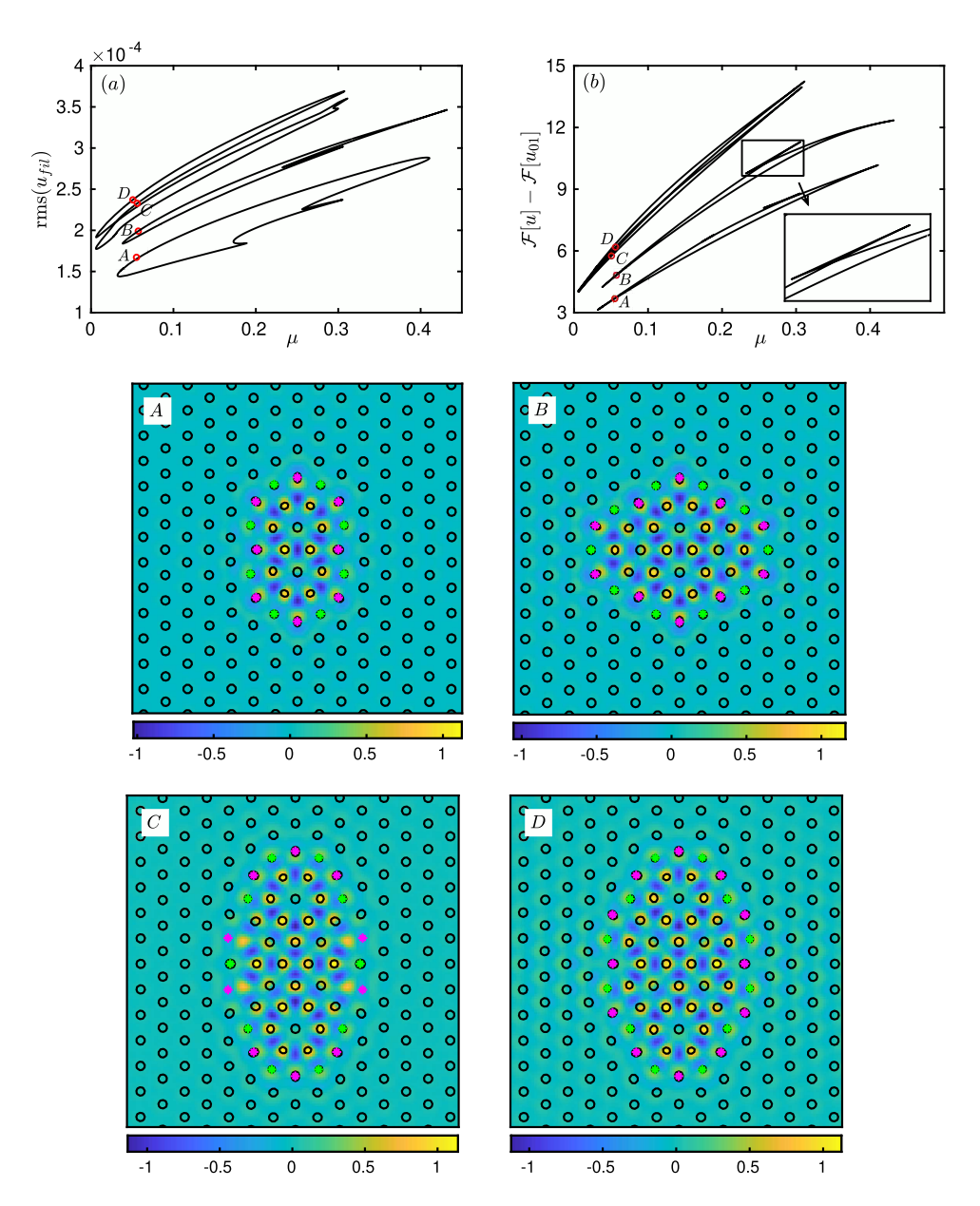


Fig. 8. Isolas of the solution branches shown in terms of (a)  $\operatorname{rms}(u_{fil})$  and (b) the free energy difference,  $\mathcal{F}[u] - \mathcal{F}[u_{01}]$ , both as functions of the bifurcation parameter  $\mu$ . Panels A–D show contours of the field u superimposed on  $u_{fil}$  at points indicated with red circles in panels (a) and (b). The inset in panel (b) shows an enlargement of the black rectangle showing a swallow-tail in the isola connected to state B.

In order to understand the length scale over which the strain field generated by the defect decays, we look in Fig. 9 at the cross-section of the filtered field  $u_{fil}$  along two different directions and do so for the field shown in Fig. 8, panel A. Cuts of  $abs(u_{fil})$ , i.e. the absolute value of the spectrally filtered field  $u_{fil}$ ,

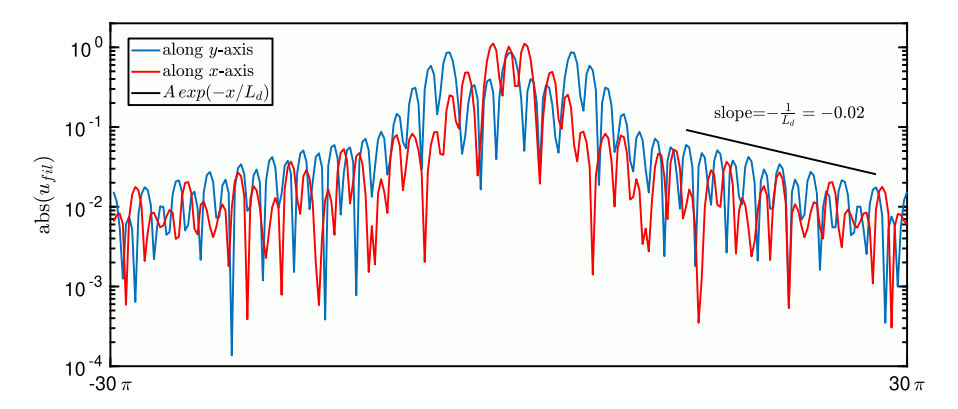


Fig. 9. Transverse cuts of  $abs(u_{fil})$ , i.e. the absolute value of the spectrally filtered field  $u_{fil}$ , along two different directions, for the field u from Fig. 8, panel A. The straight line with slope  $-1/L_d$  shows that outside the immediate grain, its influence falls off exponentially with a characteristic length scale  $L_d \sim 50$ .

along the x- and y-directions both show large values at the centre of the domain with long oscillating exponential tails. From the slope of the decay, we estimate the decay length  $L_d$  to be approximately 50, i.e. several times the pattern length scale  $(2\pi)$ . We mention that exponential localization is expected of the subcritical regime  $\mu < 0$ , even in sheared situations (Gibson & Brand, 2014; Brand & Gibson, 2014) but not necessarily for the localized axisymmetric spots that are present in SH23 in this regime (Lloyd & Sandstede, 2009).

We next turn to an example where defect states do snake, instead of lying on a stack of isolas, as in Fig. 8. Our example comes from a related but mass-conserving PFC model that forms patterns at two length scales. The model describes crystallization of soft matter into complex patterns and is closely related to the Swift–Hohenberg equation (2.1) suitably modified to generate instability at two length scales instead of just one. The model has been shown to produce both extended and spatially localized dodecagonal quasicrystals in 2D and icosahedral quasicrystals in 3D. See Subramanian *et al.* (2016) and Subramanian *et al.* (2018) for details. The model describes the evolution of a scalar density-like field  $u(\mathbf{x})$  and contains a parameter  $\sigma_0$  that controls length scale selectivity, with more negative values of  $\sigma_0$  corresponding to sharper selectivity. As we follow the branch of fully nonlinear dodecagonal quasicrystal solutions (Fig. 10, leftmost inset) for increasing  $\sigma_0$  the system starts to form localized hexagonal inclusions within the quasicrystal representing defects. Once such defects are present, the solution branch undergoes snaking as shown in Fig. 10 where the norm ||u|| is plotted as a function of  $\sigma_0$ .

The RLVs for a quasicrystalline pattern are drawn from two circles of wavevectors and the higher-order RLVs introduce new length scales at both ever larger wavevectors and at wavevectors close to zero, including wavevectors close to the first order RLVs (Rucklidge & Rucklidge, 2003; Subramanian et al., 2021). Therefore, the construction of the correct filter matrix  $\mathcal{P}$  in the case of a quasicrystalline reference pattern is rather more complex. We therefore choose a fixed reference state at  $\sigma_0 = -8.94$  and use this state to visualize the changes that occur in the field u with increasing  $\sigma_0$ . We then identify points along different parts of the snaking curve (identified by red crosses in Fig. 10 and labelled) where we plot the field u (left panels) side by side with the spectrally filtered rms( $u_{fil}$ ) calculated with respect to the reference state (right panels).

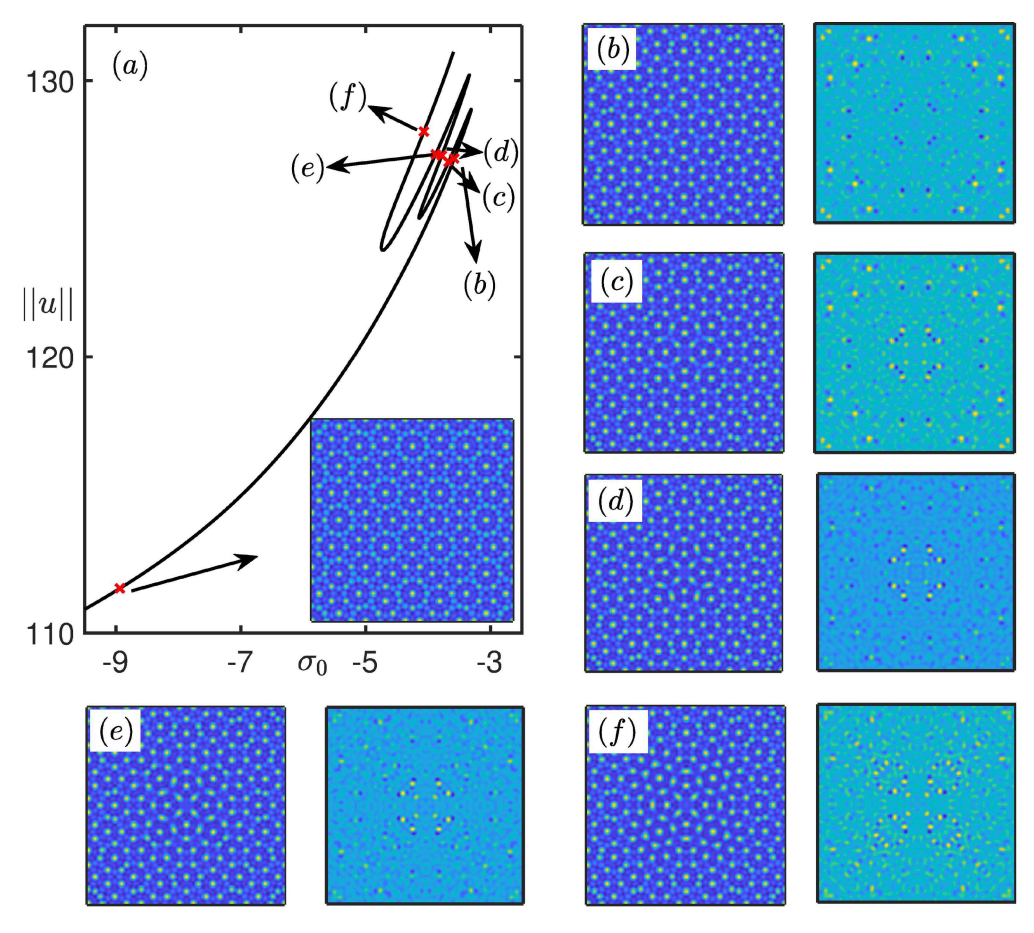


Fig. 10. (a) Solution branch of dodecagonal quasicrystals in a conserved PFC model for soft matter crystallization showing the norm of the density-like field u as a function of the bifurcation parameter  $\sigma_0$ . The inset at the bottom right shows the chosen reference state with  $\sigma_0 = -8.94$ . Panels (b)–(f) show the full field (left) and the filtered field  $u_{fil}$  relative to the reference state (right) at points marked with red crosses along the snaking solution branch (arrows). Values of the other parameters in the model are:  $\mu = \nu = -0.412$ , Q = 2 and  $q = (1/2) \cos(\pi/12)$ . For details of the model, see Subramanian *et al.* (2016).

The left inset panels in each pair show that as we move higher up the snaking branch more of the region is covered by hexagonal patches, while the right inset panels display prominent peaks at locations where there is a change from quasicrystalline to hexagonal local ordering. We note that these right panels are not as flat as the  $rms(u_{fil})$  states that we obtained in the SH23 system for PHDs. This is due to several reasons: the complex way in which RLVs add new length scales for quasicrystalline patterns at higher orders, the choice of the reference state, etc. As a result, this analysis remains incomplete but we use it here to highlight the fact that fully nonlinear equilibria with defects can indeed snake, forming multiple coexisting defect structures over a parameter interval, and leave a more detailed study of this system to future work.

### 5. Conclusion and future work

In this paper, we have demonstrated by explicit computation on a model problem, the SH23 equation in the plane, that defects in a background hexagonal pattern come in discrete families, as expected of systems in which pinning plays an important role. In particular, we have shown that these defects lie on closed solution curves called isolas and so do not snake, in contrast to the behaviour of localized states in the subcritical parameter regime in SH23 (Burke & Knobloch, 2006; Lloyd *et al.*, 2008). In other cases, such the two-scale PFC model, the defects are associated with the presence of classical snaking behaviour.

These results suggest that defects in patterns, whether periodic or quasiperiodic, behave much like localized structures on a spatially uniform background and that they can be studied using the same techniques from pattern formation theory as already used very effectively in the study of other states. Careful demodulation, i.e. removal of the background pattern, appears to be key to identifying defects in simulations or experiments, although the nature of the background state brings its own properties into the behaviour of these states: pinning to background microstructure. This effect must be retained in any theoretical description of these defect states, precluding the use of the commonly invoked amplitude-phase decomposition.

The defects studied here are associated with grain boundaries and we have introduced these into the system by rotating the hexagonal pattern in a small part of the domain through 30°. This angle determines the number of PHDs associated with the grain boundary and hence the structure of this boundary (Hirvonen *et al.*, 2016). Since this structure is associated with the inclusion of one pattern within another, both of which have the same free energy when separately covering the plane, there is no bulk phase free energy difference to drive the growth or shrinkage of the grain boundary between the two regions of different orientation. Instead, all the energy difference between the state with two grains and a defect-free pattern is associated with the boundary itself, and in particular the PHDs introduced into the pattern. It is noteworthy that this energy is positive (Fig. 7(b)) indicating that such defect structures will not form spontaneously but that they require finite amplitude perturbations to initiate them.

The fact that the grain boundaries are associated with a positive free energy implies that the system will seek to eliminate such boundaries as much as possible—that is, by grain rotation. Since many of the observed states discussed above are dynamically stable, this implies that for the parameter values where these isolas exist, there is a free energy barrier that the system must surmount to decrease the inner grain size. In the materials science context these results show that in this parameter regime grain shrinkage is a thermally activated process. Note that PFC models have previously been applied to study grain rotation (Hüter *et al.*, 2017; Radhakrishnan *et al.*, 2012) and also other more complex grain boundary and defect dynamics that occur, e.g. when a material is sheared (Chan *et al.*, 2010). Our results identify the parameter regime where grains in a polycrystalline material are dynamically stable and hence the regime in which grain rotation is an activated process. In addition, the different states identified by our approach will be attractors in the dynamics of a polycrystalline material equilibrating over time (Trautt & Mishin, 2012).

Related to this, we emphasize a point that can clearly be seen in Fig. 7: the localized grain defect structures persist over a large range of values of the bifurcation parameter  $\mu$ . We ascribe this fact to the absence of a unique Maxwell point between the two competing patterns (recall that both have the same free energy), thereby reducing the tendency towards depinning. In related systems possessing a Maxwell point, such as SH23 in the subcritical regime, the pinning region is limited by the onset of depinning that leads to the time-dependent invasion of the higher energy state by the lower energy state. We interpret Fig. 7 as suggesting that the presence of adjacent PHDs, and in particular the observed ring structure,

stabilizes individual PHDs and suggest that this fact may explain our inability to generate isolated PHDs in this system.

Our results also reveal that the localized defect structures influence the background pattern over a region larger than the defect itself. For example Fig. 7(c) clearly shows that the perturbations in  $u_{fil}$  persist over a large part of the domain. This indicates that the perturbations due to the presence of the defects decay over length scales that are several times larger than the typical distance between peaks in the pattern. Figure 9 allows us to see precisely the decay length  $L_d$  of these correlations, showing that they fall off exponentially with distance from the defect structure.

This paper represents a first step towards understanding the multiplicity of defect states in two spatial dimensions. A number of questions remain, including

- What is the smallest stationary and/or dynamically stable defect structure that can exist?
- Can we develop other topological measures to determine local order in a pattern with defects (Motta et al., 2018)?
- How do the defect structures depend on the angle between the two hexagonal patterns (Hirvonen *et al.*, 2017) and how does this angle affect the snaking properties of these states? For example, is it possible to uncover angles for which the defect states snake, rather than lying on disjoint isolas?
- What happens if non-variational terms are incorporated in the model equation? Does this generate motion of the defect state or do the defects remain stationary and stable?
- More generally, what are implications of these structures for conserved systems and materials science in general?

We leave these questions for future work on this rich and fruitful class of problems.

# Acknowledgements

The authors would like to acknowledge interesting discussions with David Lloyd, Herman Riecke and Yuan-Nan Young.

# **Funding**

Hooke Research Fellowship (to P.S.); National Science Foundation (DMS-1908891 to P.S., E.K.); Engineering and Physical Sciences Council (EP/P015689/1 to A.J.A., EP/P015611/1 to A.M.R.).

#### REFERENCES

- BECK, M., KNOBLOCH, J., LLOYD, D. J. B., SANDSTEDE, B. & WAGENKNECHT, T. (2009) Snakes, ladders and isolas of localized patterns. *SIAM J. Math. Anal.*, **41**, 936–972.
- Brand, E. & Gibson, J. F. (2014) A doubly localized equilibrium solution of plane Couette flow. *J. Fluid Mech.*, **750**, R3.
- BURKE, J. & KNOBLOCH, E. (2006) Localized states in the generalized Swift–Hohenberg equation. *Phys. Rev. E*, **73**, 056211.
- CHAIKIN, P. M. & LUBENSKY, T. C. (1995) *Principles of Condensed Matter Physics*. Cambridge: Cambridge University Press.
- CHAN, P. Y., TSEKENIS, G., DANTZIG, J., DAHMEN, K. A. & GOLDENFELD, N. (2010) Plasticity and dislocation dynamics in a phase field crystal model. *Phys. Rev. Lett.*, **105**, 015502.

- Cox, S. M. & Matthews, P. C. (2002) Exponential time differencing for stiff systems. J. Comp. Phys., 176, 430–455.
- CROSS, M. C. & HOHENBERG, P. C. (1993) Pattern formation outside of equilibrium. *Rev. Mod. Phys.*, **65**, 851–1112. DOEDEL, E., KELLER, H. B. & KERNEVEZ, J. P. (1991) Numerical analysis and control of bifurcation problems (I): bifurcation in finite dimensions. *Int. J. Bif. Chaos*, **1**, 493–520.
- GIBSON, J. F. & BRAND, E. (2014) Spanwise-localized solutions of planar shear flows. *J. Fluid Mech.*, **745**, 25–61. HALPERIN, B. I. & NELSON, D. R. (1978) Theory of two-dimensional melting. *Phys. Rev. Lett.*, **41**, 121–124.
- HIRVONEN, P., ERVASTI, M. M., FAN, Z., JALALVAND, M., SEYMOUR, M., ALLAEI, S. M. V., PROVATAS, N., HARJU, A., ELDER, K. R. & ALA-NISSILA, T. (2016) Multiscale modeling of polycrystalline graphene: a comparison of structure and defect energies of realistic samples from phase field crystal models. *Phys. Rev. B*, **94**, 035414.
- HIRVONEN, P., FAN, Z., ERVASTI, M. M., HARJU, A., ELDER, K. R. & ALA-NISSILA, T. (2017) Energetics and structure of grain boundary triple junctions in graphene. *Sci. Rep.*, 7, 1–14.
- HÜTER, C., NEUGEBAUER, J., BOUSSINOT, G., SVENDSEN, B., PRAHL, U. & SPATSCHEK, R. (2017) Modelling of grain boundary dynamics using amplitude equations. *Continuum Mech. Thermodyn.*, **29**, 895–911.
- Knobloch, E. (2015) Spatial localization in dissipative systems. Annu. Rev. Condens. Matter Phys., 6, 325-359.
- KNOBLOCH, E., UECKER, H. & WETZEL, D. (2019) Defectlike structures and localized patterns in the cubic-quintic-septic Swift–Hohenberg equation. *Phys. Rev. E*, **100**, 012204.
- KORKIDI, L., BARKAN, K. & LIFSHITZ, R. (2013) Analysis of dislocations in quasicrystals composed of self-assembled nanoparticles. *Aperiodic Crystals* (S. Schmid, R. L. Withers & R. Lifshitz eds). Netherlands: Springer, pp. 117–124.
- LLOYD, D. & SANDSTEDE, B. (2009) Localized radial solutions of the Swift–Hohenberg equation. *Nonlinearity*, **22**, 485–524.
- LLOYD, D. J. B., SANDSTEDE, B., AVITABILE, D. & CHAMPNEYS, A. R. (2008) Localized hexagon patterns of the planar Swift–Hohenberg equation. *SIAM J. Appl. Dyn. Sys.*, 7, 1049–1100.
- LLOYD, D. J. B. & SCHEEL, A. (2017) Continuation and bifurcation of grain boundaries in the Swift–Hohenberg equation. SIAM J. Appl. Dyn. Sys., 16, 252–293.
- MERMIN, N. D. (1979) The topological theory of defects in ordered media. Rev. Mod. Phys., 51, 591–648.
- MOTTA, F. C., NEVILLE, R., SHIPMAN, P. D., PEARSON, D. A. & BRADLEY, R. M. (2018) Measures of order for nearly hexagonal lattices. *Phys. D*, **380–381**, 17–30.
- RADHAKRISHNAN, B., GORTI, S. B., NICHOLSON, D. M. & DANTZIG, J. (2012) Comparison of phase field crystal and molecular dynamics simulations for a shrinking grain. *J. Phys. Conf. Ser.*, **402**, 012043.
- RUCKLIDGE, A. M. & RUCKLIDGE, W. J. (2003) Convergence properties of the 8, 10 and 12 mode representations of quasipatterns. *Physica D*, **178**, 62–82.
- SONNEVELD, P. & VAN GIJZEN, M. B. (2009) IDR(s): a family of simple and fast algorithms for solving large nonsymmetric systems of linear equations. SIAM J. Sci. Comput., 31, 1035–1062.
- Subramanian, P., Archer, A. J., Knobloch, E. & Rucklidge, A. M. (2016) Three-dimensional icosahedral phase field quasicrystal. *Phys. Rev. Lett.*, **117**, 075501.
- Subramanian, P., Archer, A. J., Knobloch, E. & Rucklidge, A. M. (2018) Spatially localized quasicrystalline structures. *New J. Phys.*, **20**, 122002.
- Subramanian, P., Ratliff, D. J., Rucklidge, A. M. & Archer, A. J. (2021) Density distribution in soft matter crystals and quasicrystals. *Phys. Rev. Lett.*, **126**, 218003.
- THIELE, U., ARCHER, A. J., ROBBINS, M. J., GOMEZ, H. & KNOBLOCH, E. (2013) Localized states in the conserved Swift–Hohenberg equation with cubic nonlinearity. *Phys. Rev. E*, **87**, 042915.
- TRAUTT, Z. T. & MISHIN, Y. (2012) Grain boundary migration and grain rotation studied by molecular dynamics. *Acta Mater.*, **60**, 2407–2424.
- TSIMRING, L. S. (1995) Penta-hepta defect motion in hexagonal patterns. Phys. Rev. Lett., 74, 4201–4204.
- Tuckerman, L. S. & Barkley, D. (2000) Bifurcation analysis for timesteppers. *Numerical Methods for Bifurcation Problems and Large-Scale Dynamical Systems* (E. Doedel & L. Tuckerman eds). New York: Springer, pp. 453–466.

- van DER VORST, H. A. (1992) Bi-CGSTAB: a fast and smoothly converging variant of Bi-CG for the solution of nonsymmetric linear systems. SIAM J. Sci. Comput., 13, 631–644.
- Woods, P. D. & Champneys, A. R. (1999) Heteroclinic tangles and homoclinic snaking in the unfolding of a degenerate reversible Hamiltonian–Hopf bifurcation. *Phys. D*, **129**, 147–170.
- ZAKHARCHENKO, K. V., FASOLINO, A., LOS, J. H. & KATSNELSON, M. I. (2011) Melting of graphene: from two to one dimension. *J. Phys. Condens. Matter*, **23**, 202202.